# A Model Study of the Stably Stratified Planetary Boundary Layer

R. A. BROST[1]

*Cooperative Institute for Research in Environmental Sciences, University of Colorado/NOAA, Boulder 80309*

J. C. WYNGAARD

*Cooperative Institute for Research in Environmental Sciences, University of Colorado/NOAA, Boulder 80309*
*and*
*Wave Propagation Laboratory, NOAA, Boulder 80302*

(Manuscript received 19 December 1977, in final form 17 April 1978)

ABSTRACT

A second-order turbulence model is used to study the stable boundary layer (SBL). Over a horizontal surface, a constant surface cooling rate drives the SBL to a steady state within a few hours. Parameterizations are developed for eddy diffusivities, the kinetic energy dissipation rate and the geostrophic drag law in this idealized case. Over a sloped surface, a constant cooling rate produces a quasi-steady-state SBL in which some flow properties continue to vary but $h(|f|/u_*L)^{\frac{1}{2}}$ becomes constant; however, this constant is a function of the wind direction relative to the slope and the baroclinity, as measured by the cooling rate times the slope. Calculated eddy diffusivity profiles in the baroclinic (sloping terrain) case compare well with recent data from Antarctica. If a surface energy budget is used rather than a constant cooling rate, the SBL does not reach a steady state even over a horizontal surface; the nondimensional height slowly decays. We conclude that equilibrium models of the SBL are likely to be much less applicable to the real world than are their counterparts for the convective boundary layer.

## 1. Introduction

The atmospheric boundary layer is often statically stable. Over land, a stable boundary layer (SBL) develops almost every night and in winter it frequently also exists during the day. Over water, an SBL is commonplace at high latitudes and over cold currents.

In this numerical study we describe the broad characteristics of an SBL which, although somewhat idealized, has many of the important features of the real-world case. We examine the influences of terrain slope, the feedback between the surface energy budget and the atmosphere, and the effect of different surfaces. A principal goal is to assess the applicability of the idealizations often made in planetary boundary layer studies (e.g., quasi-steady state, barotropic flow) to the stably stratified case.

There have been several numerical studies of the SBL, but none has adequately addressed the question of the existence of a steady state. Some claimed it did not exist; others claimed it could occur under the proper cooling conditions; still others simply assumed its existence and examined its structure.

Deardorff (1972) simulated the time evolution of a set of SBL observations using height- and stability-dependent eddy diffusivities. He concluded that the depth $h$ of the SBL was time-dependent and could not be parameterized by a diagnostic equation.

Businger and Arya (1974), also using height-dependent and stability-dependent eddy diffusivities, solved directly for the steady-state structure, and found that $h$ obeyed the diagnostic equation of Zilitinkevich (1972); however, they obtained no information on the approach to steady state.

Using a model in which the eddy diffusivities were parameterized in terms of the predicted turbulent energy, Delage (1974) found the SBL approached steady state after several hours with a realistic decaying cooling rate. He concluded that $h$ grew while the inertial velocity overshoot just above the boundary layer was growing and hence the velocity shear across the SBL was increasing, but when the shear decreased $h$ stopped growing and steady state was reached.

Wyngaard (1975) integrated a second-order turbulence numerical model and demonstrated that the SBL could approach steady state after 2–8 h, depending on the specified constant cooling rate at 1 m. He also found that $h$ obeyed Zilitinkevich's similarity prediction.

In this study, we simplify the turbulence model of Wyngaard (1975; hereafter called W75) and reduce it to a means of calculating eddy diffusivities for heat and momentum. Because the closure approximations in

[1] Current affiliation: Department of Physics and Geophysical Sciences, Old Dominion University, Norfolk, VA 23508.

0022-4928/78/1427-1440$07.00

second-order models remain somewhat controversial, we have chosen not to focus on the details of the calculated SBL structure, which can be somewhat model-dependent. Instead, our emphasis is on the gross dynamics of the SBL and the influences of real-world features such as sloping terrain and a variable cooling rate.

## 2. The model

We consider an infinite, flat, but sloped (at a small angle $\beta$ to the horizontal) surface of uniform roughness and temperature. We take the boundary layer thickness to be constant along the slope, and allow mean quantities to vary only in the direction normal to the surface ($z$) and in time. Following Lumley and Panofsky (1964), we denote the temperature, pressure and density values for an undisturbed, adiabatic atmosphere with a subscript zero. We take these as the values existing throughout the SBL at transition. Thus, for example, mean temperature $\bar{T}$ is written as $T_0+\bar{T}'$, where $\bar{T}'$ is the deviation from the adiabatic state. We choose the $x$ and $y$ directions parallel to the surface, and write the Boussinesq equations for mean wind components $U$ and $V$ in the $x$ and $y$ directions as

$$\frac{\partial U}{\partial t}=fV-\frac{1}{\rho_0}\frac{\partial \bar{P}'}{\partial x}-\frac{g}{T_0}\bar{T}'|\beta|\cos\gamma-\frac{\partial}{\partial z}\overline{uw}, \quad (1)$$

$$\frac{\partial V}{\partial t}=-fU-\frac{1}{\rho_0}\frac{\partial \bar{P}'}{\partial y}+\frac{g}{T_0}\bar{T}'|\beta|\sin\gamma-\frac{\partial}{\partial z}\overline{vw}. \quad (2)$$

Here $\gamma$ is the angle, measured counterclockwise, from the fall-line vector (the vector perpendicular to the contour lines and pointing down the slope) to the $x$ axis. We assume the pressure gradients in (1) and (2) are independent of $z$, and define the usual geostrophic wind components $U_g$ and $V_g$ by

$$\rho_0 fU_g=-\partial\bar{P}'/\partial y, \quad \rho_0 fV_g=\partial\bar{P}'/\partial x.$$

For stable conditions $\bar{T}'$ is negative and produces a katabatic (downslope) acceleration. Thus the terrain-slope terms in (1) and (2), when added to the pressure-gradient terms, give an effective pressure gradient that depends on $z$; a similar situation exists in the baroclinic, unsloped case with a horizontal temperature gradient.

The existence of a height-dependent effective pressure gradient in the SBL over sloped terrain is well-known. It is an important component of Lettau's (1967) explanation of the nocturnal jet over the Great Plains. Also, it must be considered in any description of winds over Antarctic slopes (e.g., Ball, 1960; Dalrymple *et al.*, 1966; Mahrt and Schwerdtfeger, 1970) or over the slopes of Greenland (Schwerdtfeger, 1972).

The mean potential temperature equation is

$$\frac{\partial\Theta}{\partial t}=-\frac{\partial\overline{w\theta}}{\partial z}. \quad (3)$$

Our lower boundary condition on potential temperature is provided by either a constant cooling rate ($\partial\Theta/\partial t$) or a surface energy budget. In Section 3 we follow W75 and specify the cooling rate at $z=1$ m. Later, the ground temperature $T_g$ is calculated using the surface energy budget with one subsoil grid point, i.e.,

$$\frac{\partial T_g}{\partial t}=C_g^{-1}[F\downarrow(0)-\sigma T_g^4-\rho_0 C_p Q_0]-1.18\omega(T_g-T_s), \quad (4)$$

where $F\downarrow(0)$ is the magnitude of the (specified) downward longwave radiative flux at the surface, $T_s$ the subsoil temperature, $\rho_0 C_p Q_0$ the surface heat flux, $\omega$ the angular velocity of the earth and

$$C_g=0.95\left(\frac{\lambda C_s}{2\omega}\right)^{0.5} \quad (5)$$

with $\lambda$ and $C_s$ the soil thermal conductivity and soil heat capacity per unit volume. Eqs. (4) and (5) were developed by Bhumralkar (1975) and Blackadar (1976) and tested by Deardorff (1978). The surface fluxes of heat and momentum are calculated using transfer coefficients (Sommeria, 1976).

The turbulence equations are those discussed in W75, with the following changes:

1) The time derivatives are neglected (see Appendix B) because they are smaller than the dominant terms. For example, in the turbulent kinetic energy ($q^2/2$) equation the ratio of the production ($\sim q^3/l$) and the time derivative ($\sim q^2/\tau$) terms is of order $q\tau/l$, where $l$ is a characteristic integral scale (Tennekes and Lumley, 1972) and $\tau$ a time scale characteristic of the SBL evolution. Taking $q\approx 0.3$ m s$^{-1}$, $l\approx 10$ m and $\tau\approx 3\times 10^3$ s, we find $q\tau/l\approx 100$, so that the time change term can be neglected. Examination of the other turbulence second-moment equations indicates that this estimate also applies there.

2) The Coriolis terms are also neglected in comparison to other terms. In the turbulent velocity covariance equations, for example, the ratio of shear production terms ($\sim q^3/l$) to Coriolis terms ($\sim fq^2$) is of order $q/(fl)$. For $q\approx 0.3$ m s$^{-1}$, $l\approx 10$ m and $f\approx 10^{-4}$ s$^{-1}$, we find $q/(fl)\approx 300$ so the Coriolis terms are negligible.

3) Triple correlations are ignored because surface-layer data show they are small under stable conditions (Wyngaard and Coté, 1971).

4) We parameterize the rate of dissipation of turbulent kinetic energy per unit mass as $\epsilon\propto q^3/l$, where the turbulent length scale $l=z(1+z/l_B)^{-1}$. This is an interpolation between the limits at the wall ($l\approx z$) and at the very stable outer edge of the SBL ($l\approx l_B$). We assume that the limiting scale $l_B$ of the energy-containing eddies in a stably stratified environment is determined by the balance between inertia forces and

TABLE 1. Comparison of steady-state values of boundary-layer parameters of the current model and of Wyngaard (1975) for different cooling rates. $G=10$ m s$^{-1}$, $z_0=1$ cm.

| | Cooling rate | | | | | | | |
|---|---|---|---|---|---|---|---|---|
| | 0.2 K h$^{-1}$ | | 0.5 K h$^{-1}$ | | 1 K h$^{-1}$ | | 2 K h$^{-1}$ | |
| | Current model | Wyngaard (1975) | Current model | Wyngaard (1975) | Current model | Wyngaard (1975) | Current model | Wyngaard (1975) |
| $u_*$ (m s$^{-1}$) | 0.25 | 0.23 | 0.21 | 0.20 | 0.18 | 0.16 | 0.15 | 0.13 |
| $Q_0$ (K m s$^{-1}$) | −0.0082 | −0.0088 | −0.015 | −0.013 | −0.020 | −0.016 | −0.024 | −0.018 |
| $L$ (m) | 150 | 120 | 46 | 52 | 25 | 25 | 11 | 11 |
| $\alpha$ (deg) | 28 | 33 | 35 | 39 | 38 | 44 | 42 | 49 |
| $h$ (m) | 220 | 130 | 120 | 70 | 85 | 48 | 50 | 25 |
| $d$ | 0.36 | 0.24 | 0.39 | 0.22 | 0.40 | 0.24 | 0.39 | 0.21 |
| $h/L$ | 1.5 | 1.1 | 2.6 | 1.4 | 3.4 | 2.0 | 4.5 | 2.3 |
| $u_*/(\|f\|L)$ | 17 | 19 | 45 | 38 | 74 | 67 | 130 | 120 |

buoyancy forces (Businger and Arya, 1974; Delage, 1974; Zeman and Tennekes, 1977). Requiring these intertia forces ($\sim\sigma_w^2/l_B$) and buoyant forces $[\sim(g/T_0)\times(\partial\Theta/\partial z)l_B]$ to be of the same order gives

$$l_B^2\approx\frac{\sigma_w^2}{\frac{g}{T_0}\frac{\partial\Theta}{\partial z}}=\frac{\sigma_w^2}{\omega_B^2}, \tag{6}$$

where $\omega_B=[(g/T_0)(\partial\Theta/\partial z)]^{\frac{1}{2}}$ is the Brunt-Väisälä frequency. We used $l_B=C\sigma_w/\omega_B$, with constant $C=1.69$ chosen to give critical flux and gradient Richardson numbers near 0.20 and 0.25, respectively, in agreement with W75.

While the transformation to coordinates in the plane of the slope introduces new terms in the turbulence moment equations, our small-slope assumption insures that these new terms are negligible. The turbulence equations are listed in Appendix B, and Appendix C describes our numerical techniques.

## 3. Constant cooling rate results

### *a. Steady-state, horizontal surface*

A truly steady-state SBL, in which all parameters are independent of time, can be established by balancing the cooling through turbulent heat flux divergence and the warming through mean advection. In the simplest such case, with mean quantities varying only with $x$ and $z$, and negligible radiative flux divergence and mean vertical velocity, the mean potential temperature equation is

$$\frac{\partial\Theta}{\partial t}=0=-U\frac{\partial\Theta}{\partial x}-\frac{\partial}{\partial z}\overline{w\theta}. \tag{7}$$

This situation could be found in flow over cooler water, for example.

We will use a less stringent definition of "steady state," one which allows $\Theta$ to decrease with time but requires the other SBL parameters to be time-independent. This can be approached at night over land when the surface cools. The W75 study found that if the surface cooling rate was constant, the mean potential temperature equation (3) throughout the SBL behaved approximately as

$$\frac{\partial\Theta}{\partial t}=-\frac{\partial\overline{w\theta}}{\partial z}\approx\frac{Q_0}{h}=\text{constant} \tag{8}$$

and the important parameters of the SBL approached time-independence. W75 found this quasi-steady-state structure in 2–8 h, with the shorter times for the larger cooling rates.

Examination of the terms of the surface energy budget (4) indicates the requirements for a constant near-surface cooling rate. Our results and those of W75 indicate that $Q_0$ is approximately constant after a few hours with a constant cooling rate. Furthermore, the subsoil flux to the surface, which is proportional to $(T_g-T_s)$, must increase with time as the magnitude of $(T_g-T_s)$ increases. To balance these heat inputs the net radiative deficit of the surface $[\sigma T_g^4-F\downarrow(0)]$ must increase with time, so the downward radiative flux at the surface $F\downarrow(0)$ must strongly decrease; this can be caused by the breakup of a cloud layer or the advection of drier air aloft. Thus, naturally occurring instances of a persistent constant cooling rate seem unlikely but not impossible.

Nonetheless, a constant cooling rate conveniently produces an idealized, steady-state SBL for study. We generated five such cases with our model by using cooling rates of 0.2, 0.5, 1, 2 and 4 K h$^{-1}$.

Since our initial conditions are different from those of W75, we will not compare the detailed temporal behavior of the two models. Instead, the steady states for the same cooling rates are compared in Table 1, which shows that the models give quite similar results for most properties.

The steady-state values for the friction velocity $u_*$ and the Monin-Obukhov length $L$ are nearly identical. Thus, for the same cooling rates the two models give

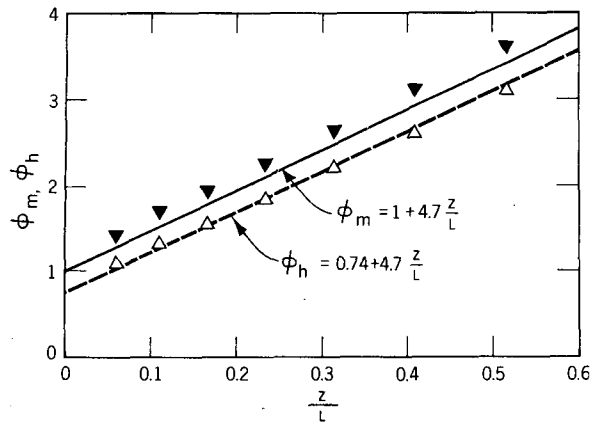


FIG. 1. Dimensionless wind shear $\phi_m$ (▼) and temperature gradient $\phi_h$ (△) for a current model run at $h/L=3.4$. Curves are parameterizations of Kansas results (Businger *et al.*, 1971).

virtually identical stabilities as measured by $\mu=u_*/(|f|L)$.

The models differ most in their equilibrium boundary layer depths. Our model predicts values of depth $h$ and the parameter $d=h(|f|/u_*L)^{\frac{1}{2}}$ about twice those of W75.

The steady-state vertical profiles of turbulence quantities from our model are so similar to those of W75 that they will not be presented here.

Fig. 1 compares calculated surface-layer profiles of nondimensional mean wind shear $\phi_m$ and nondimensional temperature gradient $\phi_h$ with the Kansas data (Businger *et al.*, 1971). The agreement of $\phi_h$ is excellent and that of $\phi_m$ is comparable with that found in model calculations by Mellor (1973), Lewellen and Teske (1973) and W75.

Fig. 2 shows the evolution of the vertical profiles of $\Theta$ and $\overline{w\theta}$ for the 1 K h$^{-1}$ cooling rate. The $\overline{w\theta}$ profiles have a slight curvature and the maximum cooling rate is near the ground. Note that the cooling between $t=5$ h and $t=10$ h at 85 m is about half that at the surface. Thus, while (8) is only crudely satisfied, the SBL is essentially in a steady state after 5 h.

In this study, as in W75, $h$ is taken as the height at which the stress is 5% of its surface value. This definition gives $h=85$ m at 10 h, whereas the potential temperature profile would indicate a greater $h$; however, the $\Theta$ profile is a product of the integrated history of $\overline{w\theta}$ and as Fig. 2 shows, the latter can extend to greater heights early in the evening. Thus the $\Theta$ profile can be a misleading indicator of $h$.

### 1) STABLE BOUNDARY LAYER DEPTH

Several simple expressions for the depth $h$ of the steady-state SBL were tested against the model results. One plausible assumption is that the bulk Richardson number across the boundary layer is a constant, say, $a_1$. If we take the bulk shear as $G/h$, with $G$ the geostrophic wind speed, and the bulk potential temperature gradient between 1 m and $h$ as $\Delta\Theta/h$, then we find

$$h=\frac{a_1G^2T_0}{g\Delta\Theta}. \tag{9}$$

However, for our model the "constant" $a_1$ varies from 0.12 to 0.34 with increasing stability. Taking $\Delta\Theta$ between $z_0$ and $h$ does not significantly improve (9); however, it is improved somewhat if $G^2$ is replaced by $(\Delta V)^2$, where $\Delta V$ is the magnitude of the difference in wind velocity between $h$ and 1 m. For fixed $G$, $\Delta V$ increases with stability because $\alpha$ and the overshoot at $h$ both increase. Nonetheless, even then $a_1$ varies from 0.11 to 0.22, and (9) remains a poor indicator of steady-state SBL depth.

A better steady-state depth equation can be derived by integrating between the surface and $z=h$ the equation of motion in the direction of the surface wind, yielding

$$h=\left(\frac{u_*}{\langle V-V_g\rangle}\right)\frac{u_*}{f}, \tag{10}$$

where $V$ and $V_g$ are the mean and the geostrophic wind components perpendicular to the surface wind, and the angle braces indicate averages over $h$. Since $V_g\equiv -G\times\sin\alpha$, we assume that $\langle V-V_g\rangle\propto G\sin\alpha$ and find

$$h=a_2u_*^2/fG\sin\alpha. \tag{11}$$

This is a fairly successful expression, in the sense that according to model results $a_2$ has no significant dependence on stability; our model gives $a_2=1.6$ and W75 gives $a_2=1.1$. Fig. 3 shows how $a_2$ converges to a steady state for the constant cooling rate runs.

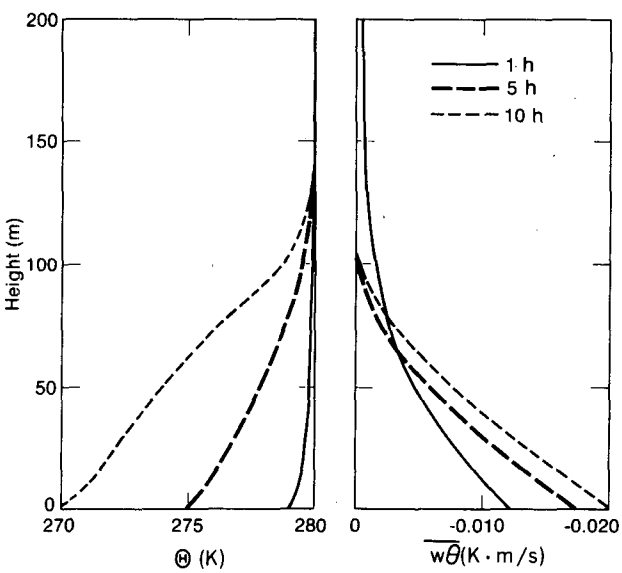


FIG. 2. Calculated time evolution of potential temperature and vertical potential temperature flux profiles for 1 K h$^{-1}$ constant cooling rate at 1 m.

Eq. (11) implies that $u_*/G=C_1(fh\sin\alpha/G)^{\frac{1}{2}}$, where $C_1=(a_2)^{-\frac{1}{2}}$; the current model gives $C_1=0.79$ and W75 gives $C_1=0.95$. The arctic observations of Carsey and Leavitt (1977) give $C_1=0.71$, but have a great deal of scatter.

Our model results show that the assumption that $\langle V-V_g\rangle \propto G\sin\alpha$ becomes very poor under baroclinic conditions. Even a slight amount of baroclinity seriously degrades the predictions of (11).

Another expression for $h$ is the similarity prediction (Zilitinkevich, 1972, 1975)

$$h=d(u_*L/|f|)^{\frac{1}{2}}. \tag{12}$$

The value of the constant $d$ depends on the definition of the depth $h$, but using the 5% stress criterion W75 found $d=0.22$; our model gives $d=0.40$, about the value found by Businger and Arya (1974). Fig. 3 shows that (12) correlates well the steady-state $h$ values from the present model over a wide range of cooling rates.

The steady-state SBL depth can be strongly model-dependent, perhaps because the height at which turbulence vanishes depends on a delicate balance between production and dissipation. As a result, minor differences in the parameterization of dissipation can yield major changes in $h$, and hence $d$. Therefore, we should not look too closely at the value of $d$; instead, we will emphasize the relative changes in $d$ caused by terrain slope or the variable surface cooling rate.

### 2) Parameterization of eddy diffusivities

The predicted steady-state profile of eddy diffusivity for momentum $K_m$ is represented well by

$$\frac{K_m}{ku_*h}=\frac{\left(\frac{z}{h}\right)\left(1-\frac{z}{h}\right)^{1.5}}{1+4.7\left(\frac{z}{h}\right)\left(\frac{h}{L}\right)}. \tag{13}$$

Note that for $z/h\ll 1$ Eq. (13) gives $K_m=ku_*z/(1+4.7z/L)$, which is the Businger *et al.* (1971) surface layer result for stable conditions. Figs. 4 and 5 illustrate the good agreement between (13) and the predictions of W75 and our model.

That the dimensionless $K_m$ should depend on only $z/h$ and $h/L$ is consistent with similarity reasoning in the steady-state case (Zilitinkevich, 1975). The similarity hypothesis would allow $\mu=u_*/(|f|L)$ to be used instead of $h/L$, since they are related in steady state through $h/L=d\mu^{\frac{1}{2}}$ [see Eq. (12)]. However, the good fit of our $K_m$ expression (13) to both sets of model results would not have occurred if $\mu$ had been used as the stability index, since the two models give different proportionality factors between $h/L$ and $\mu^{\frac{1}{2}}$ (i.e., different $d$ values). The use of $h/L$ as a stability index for stably and unstably stratified boundary layers has been suggested by Melgarejo and Deardorff (1974) and by Zilitinkevich and Deardorff (1974).

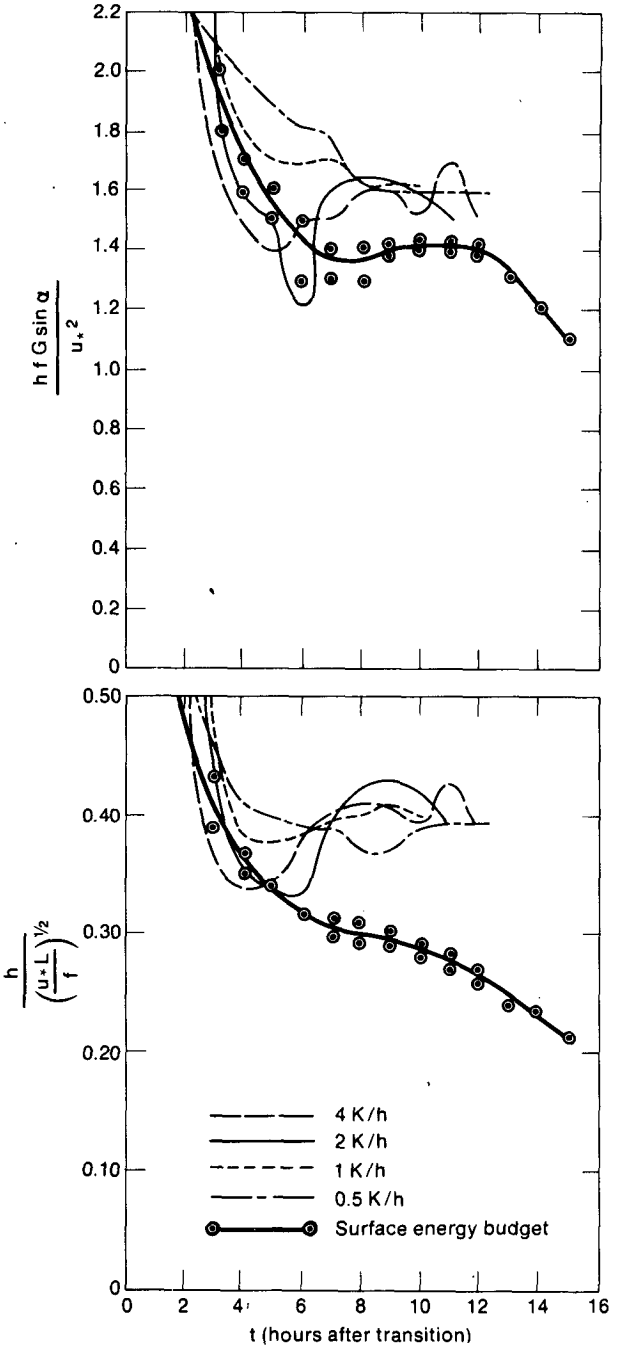


FIG. 3. Calculated time evolution of two dimensionless SBL depths. The convergence to steady state is shown for various cooling rates, along with the steady decay that results when a surface energy budget is used.

Our model results also show that $K_h/K_m$, where $K_h$ is the eddy diffusivity for temperature, averages about 1.25 in the SBL. In the surface layer it is nearer 1.35, the value implied by the lower boundary conditions, while near $h$ it is about 1.2. The W75 results show somewhat more height dependence, with $K_h/K_m\approx 1.0$ above $z\approx 0.5$ h. Thus our parameterization (13) works

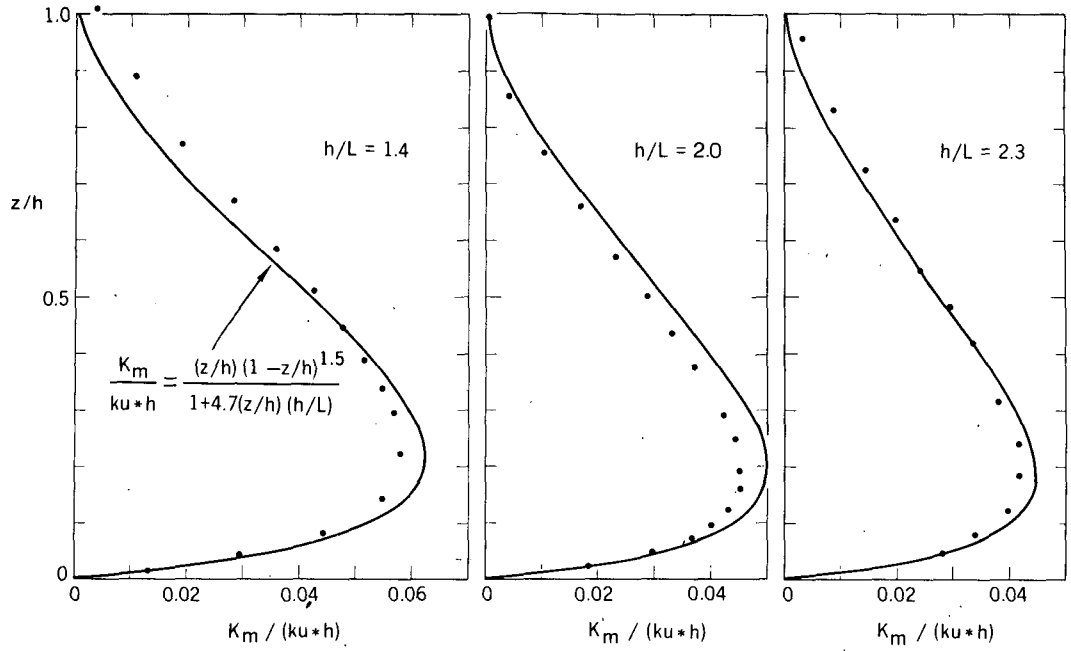


FIG. 4. Comparison of Wyngaard's (1975) predicted dimensionless steady-state $K_m$ (dots) and parameterization (13) (curves) for three cooling rates (0.5, 1 and 2 K h$^{-1}$).

about as well for $K_h$ if a factor of 1.2 is inserted on the right side.

### 3) PARAMETERIZATION OF DISSIPATION

Our model's steady-state $\epsilon$ profile is fit well by

$$\frac{\epsilon kh}{u_*^3}=\left(\frac{h}{z}\right)\left[1+3.7\left(\frac{z}{h}\right)\left(\frac{h}{L}\right)\right]\left(1-0.85\frac{z}{h}\right)^{1.5}, \quad (14)$$

as shown in Fig. 6. For $z/h \ll 1$, Eq. (14) implies that $\epsilon=[u_*^3/(kz)](1+3.7z/L)$, which as discussed in W75 is the result implied by the Businger *et al.* (1971) data and the negligible turbulent transport of energy found by Wyngaard and Coté (1971) in the stable surface layer.

We can easily derive an integral constraint for $\epsilon$. Multiplying the $x$ equation of motion (1) by $U$, the

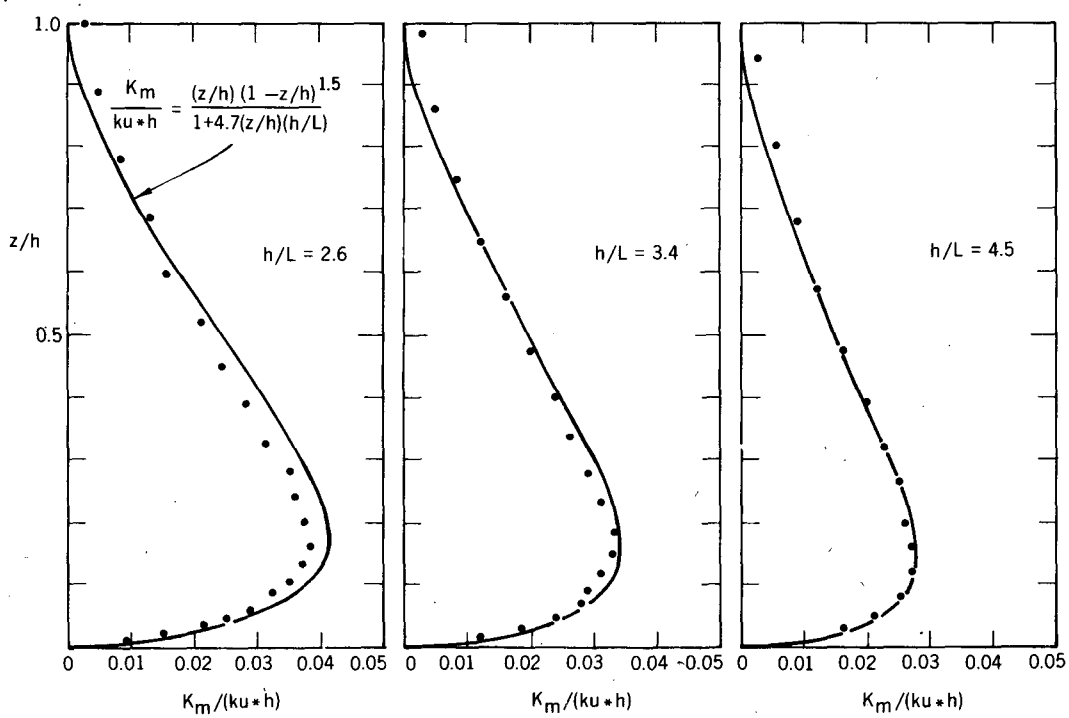


FIG. 5. As in Fig. 4 except for current model's predicted dimensionless steady-state $K_m$.

$y$ equation of motion (2) by $V$, adding, and integrating between the surface roughness height $z_0$ and $h$ gives in the steady, horizontally homogeneous, barotropic case

$$\int_{z_0}^{h}\left(U\frac{\partial\overline{uw}}{\partial z}+V\frac{\partial\overline{vw}}{\partial z}\right)dz=fG\int_{z_0}^{h}V\,dz, \quad (15)$$

where we have here chosen the $x$ axis along the geostrophic wind. The left side of (15) can be evaluated by integrating by parts and using the turbulent kinetic energy equation, yielding

$$\int_{z_0}^{h}\left(U\frac{\partial\overline{uw}}{\partial z}+V\frac{\partial\overline{vw}}{\partial z}\right)dz=-\int_{z_0}^{h}\left(\frac{g}{T_0}\overline{w\theta}-\epsilon\right)dz. \quad (16)$$

The right side of (15) can be evaluated by integrating (1), yielding

$$fG\int_{z_0}^{h}V\,dz=Gu_*^2\cos\alpha. \quad (17)$$

Combining (15)–(17) gives a kinetic energy balance for the entire layer:

$$-(h/u_*^3)[(g/T_0)\langle\overline{w\theta}\rangle-\langle\epsilon\rangle]=(G/u_*)\cos\alpha. \quad (18)$$

This constraint, with the buoyant term neglected, is also discussed by Kuhn *et al.* (1977).

If we evaluate the left side of (18) using our $\epsilon$ parameterization (14) and a linear $\overline{w\theta}$ profile, we find

$$(G/u_*)\cos\alpha=k^{-1}[\ln(h/z_0)-1.1+2.2(h/L)]. \quad (19)$$

Combining (11) and (12) yields, for the current model

$$(G/u_*)\sin\alpha=10(h/L). \quad (20)$$

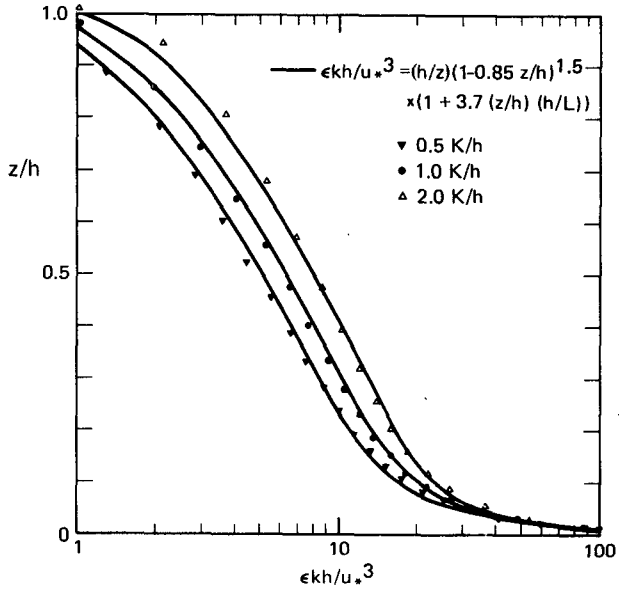


FIG. 6. Comparison of current model's predicted dimensionless steady-state $\epsilon$ and parameterization (14) (curves) for three cooling rates (0.5, 1 and 2 K h$^{-1}$).

Eqs. (19) and (20) comprise a geostrophic drag law which fits our model results (Table 1) well.

The geostrophic drag law is usually written as (Businger and Arya, 1974)

$$(G/u_*)\cos\alpha=k^{-1}[\ln|u_*/fz_0|-A], \quad (21)$$

$$(G/u_*)\sin\alpha=k^{-1}B\,\mathrm{sgn}(f), \quad (22)$$

where $A$ and $B$ depend on stability. Our model gives, from (12) and (19)–(22),

$$A=\ln(h/L)-2.2(h/L)+2.9=\tfrac{1}{2}\ln\mu-0.9\mu^{\frac{1}{2}}+2.0, \quad (23)$$

$$B=3.5(h/L)=1.4\mu^{\frac{1}{2}}, \quad (24)$$

which agrees fairly well with W75, Zilitinkevich (1975) and Arya (1977).

### *b. Sloped surface*

The "drainage" acceleration over a flat but slightly inclined surface depends on the deviation $\bar{T}'$ from the adiabatic temperature profile and hence is time-dependent. In general, this acceleration can cause $L$, $u_*$, the surface temperature flux $Q_0$, the angle $\alpha$ between the geostrophic wind and the low level flow and $h$ to change with time. However, this acceleration is impressed throughout the SBL directly as a body force, rather than diffused from the lower boundary (e.g., as is the acceleration due to changing surface friction). The model results indicate that the SBL over sloped terrain can reach a quasi-steady state in which $d=h(|f|/u_*L)^{\frac{1}{2}}$ is approximately constant; however, $d$ depends on the wind direction relative to the slope and the magnitude of the baroclinity.

Fig. 7 illustrates the evolution of several significant properties of the SBL over terrain with a slope of 0.002 and a cooling rate of 2 K h$^{-1}$. For comparison, the results are also shown for the same cooling rate over a horizontal surface. The sloped case is shown for four geostrophic wind directions relative to the fall line vector. As an example, for the Great Plains, where the surface slopes downward going from west to east, 0° represents a geostrophic wind from the west, 90° is a wind from the south, 180° is east and 270° is north. Not surprisingly, the horizontal (barotropic) case is almost always intermediate between the baroclinic extremes.

Note from Fig. 7 that $L$, $u_*$ and $Q_0$ are strongly affected by the orientation of the terrain slope. The 0° and the 270° cases are the least stable (largest $L$) because they represent downslope upper-level and low-level flow, respectively, and therefore have stronger winds near the surface. The 90° case is the most stable (smallest $L$) because its low-level flow is opposed by the downslope acceleration. This tends to minimize wind shear and turbulence production.

The SBL depths shown in Fig. 7 vary less with time than any of the other quantities we have just examined, and the dimensionless depths are even more nearly constant. At least up to 9 h, there is a perfect corre-

spondence between $h$ and the angle $\alpha$, where $\alpha$ is a crude measure of velocity shear and hence turbulence production. However, by 9 h the much greater low-level wind, and hence $u_*$, of the 270° case makes up for its smaller directional shear and the 270° height curve overtakes the 180° curve. Delage (1974) also noted a strong correlation between wind shear across the SBL and boundary layer growth.

Kuhn *et al.* (1977) integrated observed vertical profiles of geostrophic departure to obtain stress and hence eddy diffusivity profiles for five stability and wind direction classes over sloped terrain in Antarctica. Using the observed mean winds and temperatures at 0.5 and 1.0 m we estimated the gradient Richardson number Ri and inverted $\mathrm{Ri}=[0.74z/L+4.7(z/L)^2]/(1+4.7z/L)^2$ (Businger *et al.*, 1971) to obtain $z/L$ and hence $L$, using $z=0.75$ m. We compare our horizontal-surface parameterization of $K_m$ in Eq. (13) with these sloped surface observations in Fig. 8. (One class is not shown because the observed Ri at 0.75 m exceeded 1/4.7.) To see if the consistent overprediction of (13) is due to terrain slope, Fig. 9 compares (13) and the model predictions for the four sloped cases of Fig. 7. The wind directions of Kuhn *et al.* (1977) vary by only 40° and, considering the different hemispheres, the 270° case in Fig. 9 should be most similar to the observations (Fig. 8), which is the case. (We are ignoring differences in slope and latitude and only making a qualitative comparison since our estimates of $L$ for the Kuhn *et al.*, observations are relatively crude.)

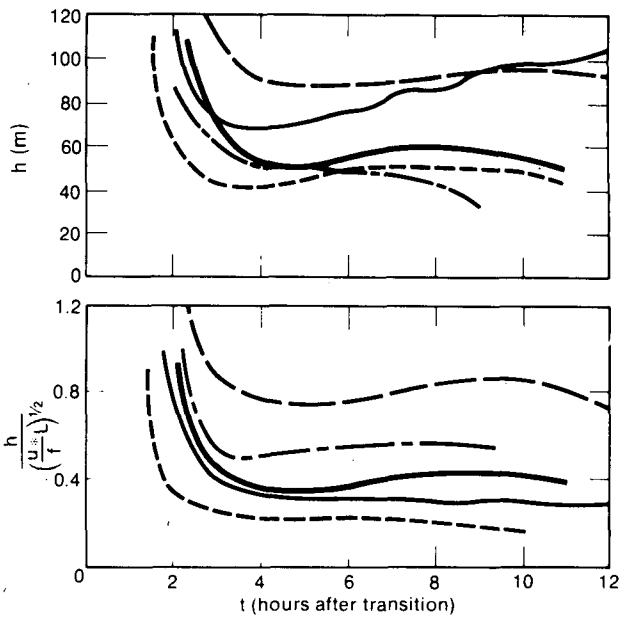


FIG. 7. Time evolution of key SBL parameters for a 2 K h$^{-1}$ cooling rate over a horizontal surface, and for four values of the angle ($\gamma$) between the fall line vector and geostrophic wind for a surface with slope 0.002.

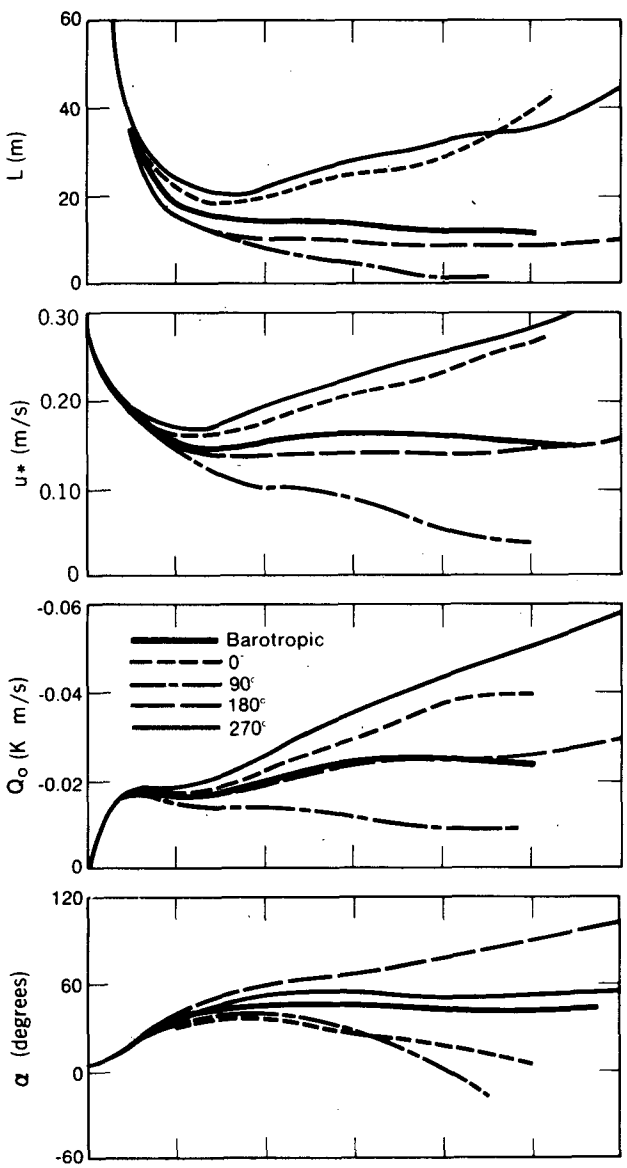


The baroclinic terms in the mean horizontal momentum equations (1) and (2) depend on the product of the temperature deficit $\bar{T}'$ and the terrain slope $\beta$. Other things being equal, $\bar{T}'$ is proportional to the near-surface cooling rate. A baroclinic parameter $B$ might be defined as

$$B=-\left(\frac{\partial\Theta}{\partial t}\right)_{1\,\mathrm{m}}\cdot\beta\ [\mathrm{K\ h^{-1}}]. \tag{25}$$

Fig. 10 depicts the time evolution of several key boundary-layer parameters for three different runs that have the same slope orientation, $\gamma=180°$, and the same baroclinic parameter, $B=0.004$ K h$^{-1}$. The runs have slopes of 0.004, 0.002 and 0.001, and cooling rates of 1, 2 and 4 K h$^{-1}$, respectively. We notice that runs with the same $B$ value can have significant differences in some properties, so $B$ is not an adequate indicator of slope effects.

We can look more closely at terrain-slope effects by considering the ratio ($S$) of the magnitudes of the mean drainage and friction forces

$$S \approx \frac{(g/T_0)\bar{T}'\beta}{u_*^2/h}, \tag{26}$$

and we ignore the effect of the orientation of the slope. This ratio depends on $z$, so it is not directly useful as a bulk index, but it can give us some insight. Note first that if $\beta=0.001$, $\bar{T}'=3$ K, $h=100$ m and $u_*=0.1$ m s$^{-1}$, then $S=1$; thus with a seemingly mild slope of 0.001 and typical SBL conditions, the drainage forces are of the same order as the turbulent friction. This explains why the results in Fig. 10 are so slope-dependent. Although the runs in Fig. 10 have the same value of $B$, which is proportional to $\bar{T}'\beta$, their representative values of $S$ differ enough to make their flow properties evolve differently.

Fig. 10 shows that some properties (e.g., $L$, $u_*$, $h$) fairly quickly establish quasi-steady values, while $\alpha$, for example, continuously increases. This flow cannot attain a true steady state, even though some of its properties seem to, because the parameter $S$ continuously increases with time. However, in all runs $d$ converges to about the same value (0.8). Evidently $d$ is more sensitive to $\gamma$ than to $S$.

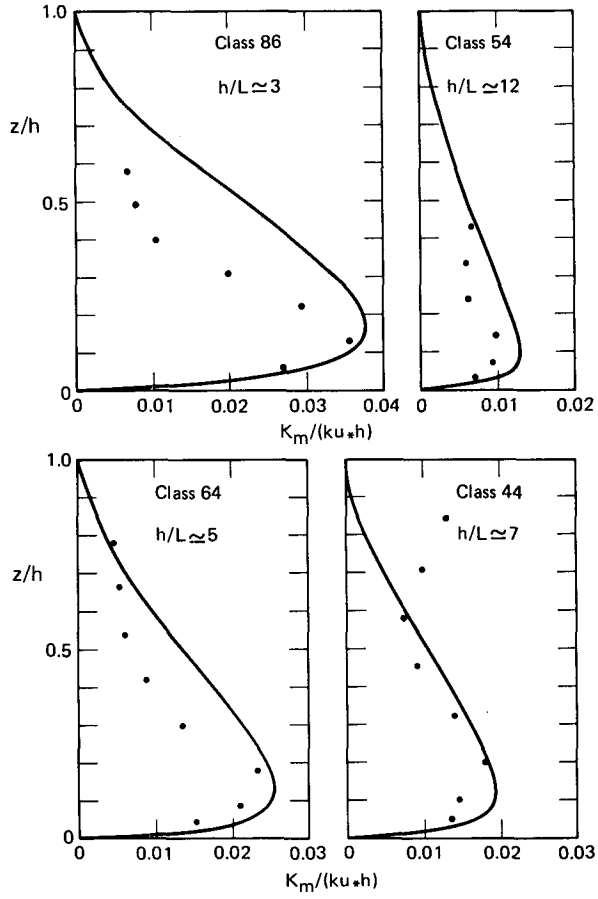


FIG. 8. Comparison of observed dimensionless $K_m$ (dots) over sloped terrain (Kuhn *et al.*, 1977) with parameterization (13) (curves), for four stability classes.

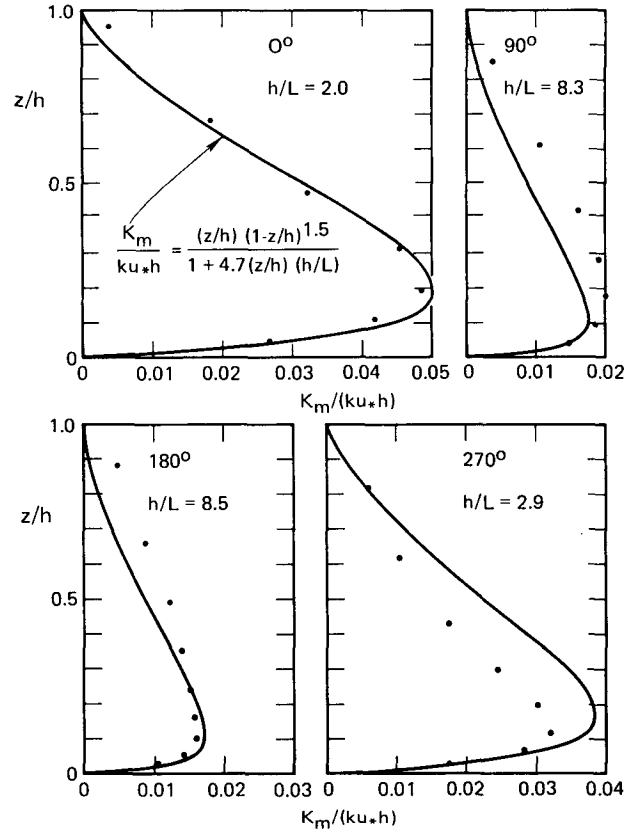


FIG. 9. Calculated dimensionless $K_m$ profiles (dots) for the four cases of Fig. 7. Curves are from (13).

We have shown (Fig. 7) that the greatest $d$ value occurs for $\gamma=180°$ and the smallest for 0°. For a baroclinic parameter $B=0.004$ K h$^{-1}$, the ratio $d_{180}/d_0$ is predicted to be 4 and for $B=0.001$ K h$^{-1}$ it is predicted to be 1.5. This comparison indicates a significant dependence of $d$ on $B$.

Predictions for the geostrophic drag coefficient $u_*/G$ as a function of the stratification parameter $\mu$ are shown in Fig. 11. The curve in Fig. 11 is the prediction obtained by squaring and adding (21) and (22), using our parameterizations (23) and (24) for $A$ and $B$, for a surface Rossby number $G/(|f|z_0)=10^7$. The current model predictions for the horizontal surface case lie on this curve, while the W75 results are slightly below it. (The models would have disagreed strongly had $h/L$ been used as the stability parameter.) Had the sloped-terrain results been plotted in the normal way, they would not have followed the curve well. Instead, for these cases a drag coefficient based on a $G$ calculated from the depth-averaged "effective" pressure gradient was used, and these results follow the barotropic prediction quite well. This use of the layer-averaged

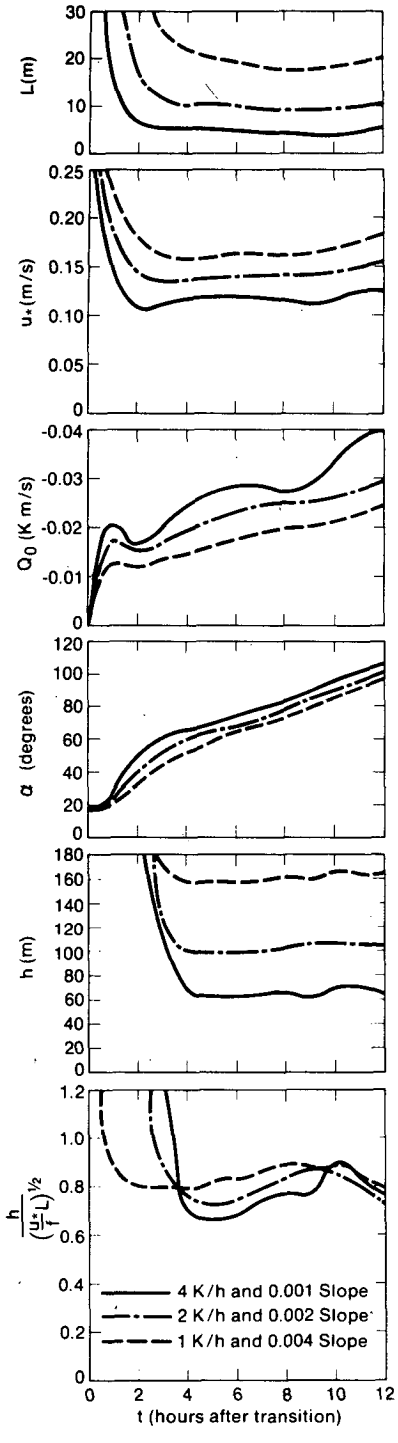


FIG. 10. Time evolution of key SBL parameters for three model runs with $\gamma=180°$ and $B=0.004$ K h$^{-1}$.

geostrophic wind in the baroclinic case has also been suggested for the convective boundary layer (Arya and Wyngaard, 1975).

## 4. Surface energy budget

We now use a surface energy budget (Blackadar, 1976), rather than an imposed constant cooling rate at 1 m. In the previous sections this cooling rate was the key variable determining the stratification. The situation now is much more complex as the cooling rate is replaced by several parameters:

1) The temperature difference $\Delta T$ between the initial adiabatic atmosphere and subsoil slab. We have tested temperature differences that ranged from $-0.5$ to $+20$ K.

2) The heat capacity $C_g$ (per unit area) of the subsoil slab, which enters as the parameter $C_g/(\rho_0 C_p)$ with $\rho_0$ and $C_p$ the density and specific heat of the air. We have used values of $C_g/(\rho_0 C_p)$ corresponding to a poor conductor (snow, 10 m) and an excellent conductor (rock, 221 m). These values of $C_g/(\rho_0 C_p)$ were chosen following Blackadar (1976). From (5), they correspond approximately to $\lambda=0.2\times10^{-3}$ cal (cm s K)$^{-1}$ and $C_s=0.09$ cal (cm$^3$ K)$^{-1}$ for snow and $\lambda=10^{-2}$ cal (cm s K)$^{-1}$ and $C_s=0.6$ cal (cm$^3$ K)$^{-1}$ for rock (Geiger, 1966).

3) The imposed downward long wave radiative flux at the surface. We used values of $F\downarrow(0)/(\rho_0 C_p)$ from 16 to 24 K m s$^{-1}$.

When the surface energy budget is used, the cooling rate of the surface becomes a strong function of time. Initially it is large, making the boundary layer very stable and shallow; however, after 1 or 2 h, $L$ begins to increase again as the cooling rate declines. These variable conditions are not transmitted directly to the fluid as is the body force causing downslope acceleration in the sloping-terrain case. Instead, information about the changing surface conditions (e.g., $u_*$ and $L$) must diffuse into the SBL from below. We can crudely estimate this diffusion time as of the order of $h^2/K_m$. From Figs. 4 and 5, we take a typical $K_m$ value representative

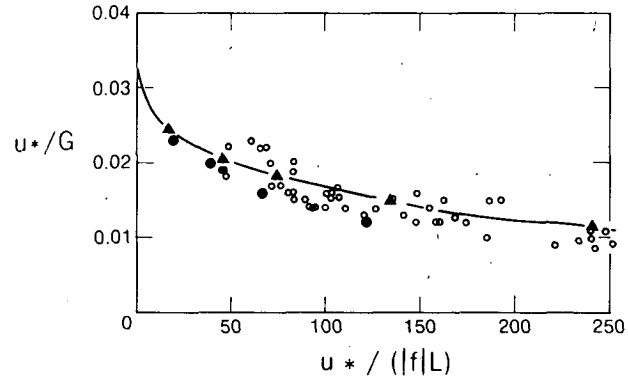


FIG. 11. Stability variation of geostrophic drag coefficient, from model simulations with a constant surface cooling rate. Curve, from Eqs. (21)–(24); (▲) current model results for horizontal terrain; (●) W75 model results; (○) current model results, sloping terrain, $G$ based on layer-averaged effective pressure gradient.

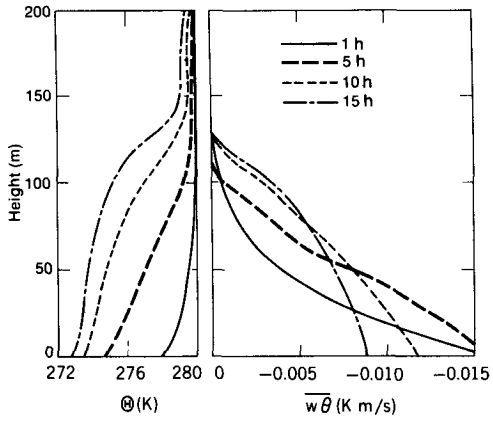


FIG. 12. Calculated time evolution of $\Theta$ and $\overline{w\theta}$ profiles for surface energy budget (4) case using $G=10$ m s$^{-1}$, $\Delta T=5$ K, $C_g/(\rho_0 C_p)=221$ m and $F\downarrow(0)/(\rho_0 C_p)=20$ K m s$^{-1}$.

of the layer as a whole as $K_m \approx 0.03 k u_* h$. If $u_*=0.1$ m s$^{-1}$ and $h=100$ m, we find $h^2/K_m \sim 10^5$ s or $\sim 30$ h. By contrast, a convective boundary layer would be expected to respond to changing surface conditions with a time scale $h^2/K_m \approx h/w_*$, where $w_*=[(g/T_0)Q_0 h]^{\frac{1}{3}}$ is the convective velocity scale. Under typical conditions we might have $h \approx 10^3$ m, $w_* \approx 2$ m s$^{-1}$, so $h/w_* \approx 10$ min. Thus, while the convective boundary layer is often quasi-steady, this suggests the SBL probably only rarely is. As evidence of this, note the different behavior of the dimensionless SBL depth in Fig. 3 when a surface energy budget is used.

As an aside, we note that the slowness of the response of the current model to changing surface conditions is not due to the lack of turbulent transport terms in the turbulence equations because we could find no consistent differences in response time between the current model and W75, which has these terms.

Fig. 12 illustrates the evolution of the potential temperature and potential temperature flux profiles for a case with $G=10$ m s$^{-1}$ and $\Delta T=5$ K. This should be contrasted with Fig. 2 which shows the evolution of the same variables under constant cooling rate conditions. With a constant near-surface cooling rate, the cooling rate (turbulent heat flux divergence) initially decreases strongly with height, but by 10 h the cooling is approximately constant with height. With a surface budget, the height of the maximum cooling rate increases with time, creating a tendency to develop a uniform layer with a large potential temperature jump at the top. The $\Theta$ and $\overline{w\theta}$ profiles are curved instead of quasi-linear and the curvature changes with time. The relatively large temporal changes in the magnitudes and curvatures of the $\Theta$ and $\overline{w\theta}$ profiles indicate that this case does not attain steady state.

Fig. 13 illustrates the evolution of the surface temperature drop for an initially adiabatic atmosphere at 280 K and a surface initially at 279 K. For a fixed, imposed downward longwave radiative flux at the surface (20 K m s$^{-1}$) and the same surface characteristics $[C_g/(\rho_0 C_p)=221$ m], there are four curves (I, G, D, C) corresponding to different temperature drops (2.5, 5, 10 and 20 K) between the initial adiabatic atmosphere and the subsoil slab. The extent to which the surface temperature drops below the subsoil temperature depends on the surface radiative deficit and hence on the absolute temperature; thus, in the 2.5 K case (curve I) the surface temperature drops almost 3 K below the subsoil temperature whereas in the 20 K case (C) it drops only 0.5 K below. For the 5 K case (G) the effects of varying the imposed downward flux and using different surface characteristics are shown. If a larger downward radiative flux is used (H) the surface temperature obviously will not decrease as much below the subsoil temperature. If the soil has a $C_g/(\rho_0 C_p)$ value characteristic of snow (B), the surface temperature drops well below (15 K) the subsoil temperature. This curve has a bump due to complex feedback between the atmosphere and the surface.

Several simple analytical theories have been developed to predict the surface or shelter temperature fall at night (Haltiner and Martin, 1957, p. 131). For

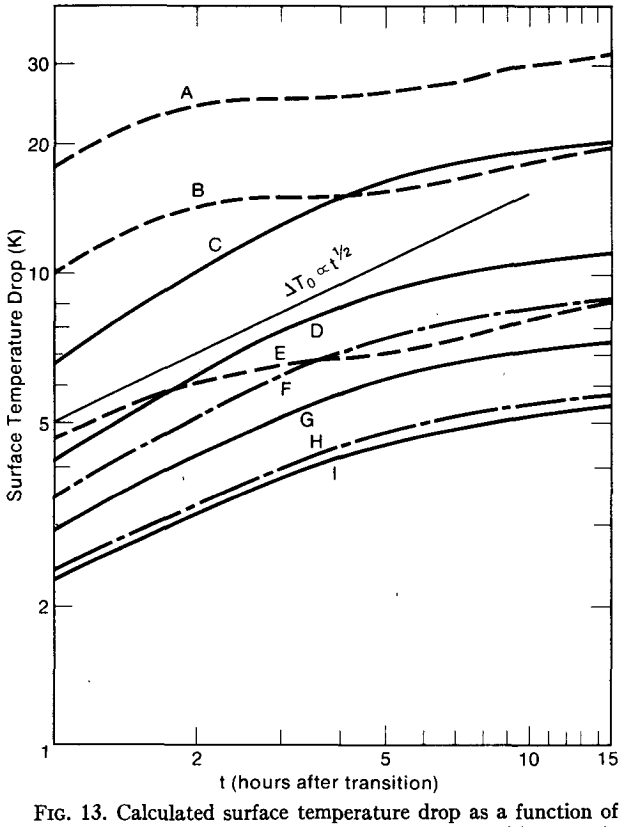


FIG. 13. Calculated surface temperature drop as a function of time for simulations using surface energy budget (4). Run A, $\Delta T=5$ K, $C_g/(\rho_0 C_p)=10$ m, $F\downarrow(0)/(\rho_0 C_p)=16$ K m s$^{-1}$; run B, 5 K, 10 m, 20 K m s$^{-1}$; run C, 20 K, 221 m, 20 K m s$^{-1}$; run D, 10 K, 221 m, 20 K m s$^{-1}$; run E, 5 K, 10 m, 24 K m s$^{-1}$; run F, 5 K, 221 m, 16 K m s$^{-1}$; run G, 5 K, 221 m, 20 K m s$^{-1}$; run H, 5 K, 221 m, 24 K m s$^{-1}$; run I, 2.5 K, 221 m, 20 K m s$^{-1}$.

example, Brunt (1939) assumed that the net radiative deficit at the surface was constant and that this deficit was balanced by the soil heat flux alone. He found that the surface temperature drop varied as the square root of time. The theory was subsequently generalized to include the atmospheric heat flux, but the functional dependence on temperature was unchanged if a constant eddy diffusivity was used for heat transfer. [A comparison with Groen (1947), whose theory is more realistic than that of Brunt (1939), though less so than the present study, was not made because it could not be definitive. This is because the cooling in Groen (1947) depends on the assumed value of the derivative with respect to temperature of the net radiative flux at the surface, while here it depends on $\Delta T$ and $F\downarrow(0)$.]

Fig. 13 shows that for $C_g/(\rho_0 C_p)=221$ m and for a $\Delta T$ of 5 or 10 K (G or D), the surface temperature drop in our model does indeed follow $t^{\frac{1}{2}}$ for the first 3 or 4 h. For the same surface and a larger temperature drop of 20 K (C), the initial tendency is slightly greater. For a smaller temperature drop of 2.5 K (I), the initial tendency is less. For all cases, the present model's predicted rate of temperature drop eventually falls below $t^{\frac{1}{2}}$ as the net radiative deficit at the surface decreases.

The similarity between Brunt's prediction and ours should be greatest for a surface where the ratio of the soil heat flux to the atmospheric heat flux is maximized, e.g., soil with large thermal diffusivity and heat capacity, as in the surface just discussed. If the surface used had a low $C_g/(\rho_0 C_p)$ value, such as that for snow, then the fact that the eddy diffusivity in the air was not constant, as assumed in an extension of Brunt, but was a function of time, as in our model, would be important. Thus, our model's more realistic representation of atmospheric physics should be more important for curves A, B and E. These curves depart from $t^{\frac{1}{2}}$ behavior sooner and more drastically and have a more complicated temporal behavior.

## 5. Conclusions

This study supports the findings of W75 that a constant cooling rate imposed near a horizontal lower boundary can drive the boundary layer to steady state within a few hours. Although the steady-state layer depth $h$, together with the changes in speed and potential temperature across the layer, do not give the same bulk Richardson number for all cases, $h$ is uniquely related to other SBL parameters. Calculated eddy diffusivity profiles and drag coefficients agree well with recent observations in the arctic and antarctic.

The scaled SBL depth $d=h(|f|/u_*L)^{\frac{1}{2}}$ over a sloped surface with a constant cooling rate has different steady-state values depending on the wind direction relative to the slope. The slope effect is strong; for example, $d$ varies by a factor of 4 for a slope of 0.002 and a cooling rate of 2 K h$^{-1}$.

When the lower boundary condition on temperature is provided by a surface energy budget rather than a constant cooling rate, the SBL typically does not reach steady state. The surface temperature drop behaves as $t^{\frac{1}{2}}$ for the first few hours, but eventually decreases more slowly. This failure to reach steady state is due to the slowness of the SBL to adjust to the changing surface conditions.

In addition, we conclude that the real SBL is subject to other influences that greatly complicate its structure and dynamics. First, our finding that $h$ is very sensitive to model parameterizations suggests it can also be affected strongly by turbulence created by unstable gravity waves. Wave-turbulence interactions and their influence on SBL structure remain an important but relatively unexplored problem.

Second, we showed that even slight terrain slopes have strong effects on the SBL. However, real terrain is much more complicated than our constant-slope model, having a spectrum of slopes; the extent to which this affects SBL structure is also unknown.

Finally, we may have missed important features of the SBL because we could not model a full diurnal cycle. We started with balanced, steady-state, slightly stable initial conditions at transition. A more realistic initial condition for the wind would be an imbalance or inertial oscillation dependent on the history of the flow; this inertial oscillation could be important in the growth of the SBL. Also, we compared the SBL development over different soils and with different initial temperature differences between the adiabatic atmosphere and the subsoil slab. It would be valuable to compare full daily cycles over different soils such that the initial temperature difference would depend on the differing storage in the soil and the differing heating of the atmosphere.

*Acknowledgments.* We are grateful to J. W. Deardorff, J. Businger, W. Hooke, D. Lilly, W. Neff, K. S. Rao, B. Stankov and O. Zeman for helpful discussions, and to Ms. J. Trebing for patiently and skillfully typing many revisions of the manuscript.

## APPENDIX A

### Table of Symbols

| | |
|---|---|
| $B$ | baroclinic parameter [$=-(\partial\Theta/\partial t)\beta$] |
| $C_g$ | heat capacity per unit area of soil slab [Eq. (5)] |
| $C_p$ | specific heat of air at constant pressure |
| $d$ | scaled SBL depth [Eq. (12)] |
| $f$ | Coriolis parameter, taken as $10^{-4}$ s$^{-1}$ in model |
| $F\downarrow(0)$ | magnitude of the downward longwave radiative flux at the surface |
| $g$ | gravitational acceleration |
| $G$ | geostrophic wind speed |
| $h$ | height of SBL, i.e., height at which stress declines to 5% of surface maximum |
| $k$ | von Kármán constant, taken as 0.35 in model |

$K_m$, $K_h$ eddy diffusivity for momentum, temperature
$l$ integral length scale
$l_B$ asymptotic value of $l$ $[=C\sigma_w/\omega_B]$
$L$ Monin-Obukhov length $[=-u_*^3T_0/(kgQ_0)]$
$\bar{P}'$ deviation of mean pressure from background state $P_0$
$q$ turbulent velocity scale $[=(\overline{u_iu_i})^{\frac{1}{2}}]$
$Q_0$ surface potential temperature flux
Ri gradient Richardson number

$$\left\{=\frac{g}{T_0}\frac{\partial\Theta}{\partial z}\Big/\left[\left(\frac{\partial U}{\partial z}\right)^2+\left(\frac{\partial V}{\partial z}\right)^2\right]\right\}$$

$T_g$ surface temperature
$T_0$ adiabatic background temperature of atmosphere
$T_*$ scaling temperature $[=-Q_0/u_*]$
$T_s$ temperature of subsoil slab
$\bar{T}'$ deviation from adiabatic background temperature
$\Delta T$ temperature difference between initial atmosphere and subsoil slab $[=T_0-T_s]$
$\Delta T_0$ surface temperature drop $[=T_0-T_g]$
$U_i$ mean velocity $(U,V,W)$
$u_i$ fluctuating velocity $(u,v,w)$
$u_*$ surface friction velocity
$z_0$ surface roughness length, taken as 0.01 m in model
$\alpha$ angle between geostrophic and surface winds
$\beta$ surface slope
$\gamma$ angle of geostrophic wind relative to fall line vector
$\Theta$ mean potential temperature
$\theta$ fluctuating potential temperature
$\Delta\Theta$ mean potential temperature increase across SBL
$\Theta_v$ mean virtual potential temperature
$\mu$ stability index $[=u_*/(|f|L)]$
$\rho_0$ density of air in background adiabatic state
$\sigma$ Stefan-Boltzmann constant
$\sigma_w$ root-mean-square vertical velocity
$\phi_h$ nondimensional potential temperature gradient $[=(kz/T_*)(\partial\Theta/\partial z)]$
$\phi_m$ nondimensional velocity gradient $[=(kz/u_*)\times(\partial U/\partial z)]$
$\omega_B$ Brunt-Väisälä frequency $\left[=\left(\frac{g}{T_0}\frac{\partial\Theta}{\partial z}\right)^{\frac{1}{2}}\right]$

## APPENDIX B

## The Diagnostic Turbulence Equations

Our turbulence equations are derived from those of W75 by neglecting the time change, Coriolis and turbulent transport terms, and by using only some of the full set of equations. The reader is referred to that paper for a full discussion of the parameterizations. The closure constants and lower boundary conditions were unchanged except in a few instances where slight modifications were required because of the model simplifications. Our equations follow:

*Vertical velocity variance*

$$0.30\left(\overline{uw}\frac{\partial U}{\partial z}+\overline{vw}\frac{\partial V}{\partial z}\right)$$
$$=0.67(g/T_0)\overline{w\theta}-0.093q^3/l-0.51q(\overline{w^2}-q^2/3)/l.$$

*Turbulent kinetic energy*

$$\overline{uw}(\partial U/\partial z)+\overline{vw}(\partial V/\partial z)=(g/T_0)\overline{w\theta}-0.139q^3/l.$$

*Shear stress*

$$\left.\begin{aligned}0.14\overline{w^2}(\partial U/\partial z)&=-0.255(\overline{uw}q/l)+0.28(g/T_0)\overline{u\theta}\\0.14\overline{w^2}(\partial V/\partial z)&=-0.255(\overline{vw}q/l)+0.28(g/T_0)\overline{v\theta}\end{aligned}\right\}.$$

*Heat flux*

$$\overline{w^2}(\partial\Theta/\partial z)=-1.35\overline{w\theta}q/l+(1-C_1)(g/T_0)\overline{\theta^2}$$

where
$$C_1=\begin{cases}0.5+1.5\ \mathrm{Ri}^2-\mathrm{Ri}^3, & 0<\mathrm{Ri}<1\\ 1, & \mathrm{Ri}>1\end{cases}$$

$$\overline{uw}(\partial\Theta/\partial z)+0.5\overline{w\theta}(\partial U/\partial z)=-1.35\overline{u\theta}q/l,$$
$$\overline{vw}(\partial\Theta/\partial z)+0.5\overline{w\theta}(\partial V/\partial z)=-1.35\overline{v\theta}q/l.$$

*Temperature variance*

$$2\overline{w\theta}(\partial\Theta/\partial z)=-0.386\overline{\theta^2}q/l.$$

## APPENDIX C

## Numerical Methods

The Adams-Bashforth finite-difference scheme was used to march in time. The vertical grid was equally spaced in the transformed variable $\eta$, where

$$\eta=\frac{z}{A_1}+\ln\frac{z+A_2}{A_2}.$$

Here $A_2$ controls the rate at which the logarithmic grid expands near the surface, while $A_1$ determines the height at which the grid became linear. Values of $A_2=5$ m and $A_1=250$ m were used. The variables were staggered in the vertical with the mean and turbulence quantities calculated on different but interlacing grids.

The computer model was a factor of 10 faster than that of W75 because we used simpler equations, time step control (Zeman and Lumley, 1976), and a grid with variable resolution and vertical extent.

Because spatial rather than temporal resolution limited the accuracy of our solutions, the full set of turbulence equations was not solved every time step. We used the following procedure:

1) We solved the turbulence equations (Appendix B) to form a quadratic equation for $q^2$. The largest root

always proved to be the desired solution. If Ri exceeded a critical value both roots were negative and $q^2$ was set at a small positive value.

2) All of the vertical fluxes were then calculated in terms of the known $q^2$.

3) Effective eddy diffusivities for momentum and heat were formed from these fluxes and the existing mean gradients.

4) These effective eddy diffusivities were used to calculate fluxes while ten time steps were taken with the mean equations.

5) The procedure was repeated.

We tested the accuracy of this procedure by comparing two 10 h model simulations. In one, the procedure was used and, in the other, the full turbulence set was solved each time step. After 10 h, the temperatures differed at most by 1 part in $10^5$ and all other significant quantities by no more than 1 part in $10^3$.

Our program discarded the top grid point if the stress there fell below a small threshold value for one hour. Typically, after 5 h five grid points had been discarded and the computational domain had shrunk from 500 to 250 m. Then the grid was doubled to 30 points and the mean variables were interpolated onto the new grid. The time evolution of predicted variables did not show any noticeable effects of this grid change. Before the grid change the vertical resolution was 2 m near the surface and increased smoothly to 50 m aloft; after the change it varied from 1 to 25 m.

A dissipation length scale which behaved as $l_B=C\sigma_w/\omega_B$ at large $z$ and the lack of explicit diffusion terms in the turbulence equations allowed the turbulent kinetic energy at adjacent grid points to tend to drift apart. To avoid this we introduced a small amount of diffusion by running a Hanning filter over $l(z)$.

The initial conditions were provided by holding $\Theta$ fixed with $\partial\Theta/\partial z=4\times10^{-5}$ K m$^{-1}$ and integrating to a steady state.

## REFERENCES


Arya, S. P. S., 1977: Suggested revisions to certain boundary layer parameterization schemes used in atmospheric circulation models. *Mon. Wea. Rev.*, **105**, 215–227.

——, and J. C. Wyngaard, 1975: Effect of baroclinicity on wind profiles and the geostrophic drag law for the convective planetary boundary layer. *J. Atmos. Sci.*, **32**, 767–778.

Ball, F. K., 1960: Winds on the ice slopes of Antarctica. *Proc. Symp. Antarctic Meteorology*, Melbourne, Pergamon Press, 9–16.

Bhumralkar, C. M., 1975: Numerical experiments on the computation of ground surface temperature in an atmospheric general circulation model. *J. Appl. Meteor.*, **14**, 1246–1258.

Blackadar, A. K., 1976: Modeling the nocturnal boundary layer. *Preprints Third Symp. Atmospheric Turbulence, Diffusion and Air Quality*, Raleigh, Amer. Meteor. Soc., 46–49.

Brunt, D., 1939: *Physical and Dynamical Meteorology*, 2nd ed. Cambridge University Press, 428 pp.

Businger, J. A., and S. P. S. Arya, 1974: Height of the mixed layer in a stably stratified planetary boundary layer. *Advances in Geophysics*, Vol. 18A, Academic Press, 73–92.

——, J. C. Wyngaard, Y. Izmui and E. F. Bradley, 1971: Flux-profile relationships in the atmospheric surface layer. *J. Atmos. Sci.*, **28**, 181–189.

Carsey, F., and E. Leavitt, 1977: Preliminary study of pibal and acoustic radar data over pack ice. Submitted to *J. Appl. Meteor.*

Dalrymple, P. C., H. Lettau and S. Wollaston, 1966: South Pole micrometeorology program: Data analysis. *Studies in Antarctic Meteorology*, Vol. 9, *Antarctic Res. Ser.*, Amer. Geophys. Union, 13–57.

Deardorff, J. W., 1972: Rate of growth of the nocturnal boundary layer. *Proc. Symp. Air Pollution, Turbulence and Diffusion*, H. W. Church and R. E. Luna, Eds., 183–190.

——, 1978: Efficient prediction of ground surface temperature and moisture, with inclusion of a layer of vegetation. *J. Geophys. Res.*, **83**, 1889–1903.

Delage, Yves, 1974: A numerical study of the nocturnal atmospheric boundary layer. *Quart. J. Roy. Meteor. Soc.*, **100**, 351–364.

Geiger, R., 1966: *The Climate Near the Ground*. Harvard University Press, 611 pp.

Groen, P., 1947: Note on the theory of nocturnal radiational cooling of the earth's surface. *J. Meteor.*, **4**, 63–66.

Haltiner, G. J., and F. L. Martin, 1957: *Dynamical and Physical Meteorology*. McGraw-Hill, 470 pp.

Kuhn, M., H. H. Lettau and A. J. Riordan, 1977: Stability related wind spiraling in the lowest 32 m. Meteorological Studies at Plateau Station, Antarctica. Pap. 7, *Antarctic Research Series*, Vol. 25, Amer. Geophys. Union, 93–111.

Lettau, H. H., 1967: Small to large-scale features of boundary layer structure over mountain slopes. *Proc. Symp. Mountain Meteorology*, Atmos. Sci. Pap. 122, Colorado State University.

Lewellen, W. S., and M. Teske, 1973: Prediction of the Monin-Obukhov similarity functions from an invariant model of turbulence. *J. Atmos. Sci.*, **30**, 1340–1345.

Lumley, J. L., and H. A. Panofsky, 1964: *The Structure of Atmospheric Turbulence*. Wiley, 239 pp.

Mahrt, L. J., and W. Schwerdtfeger, 1970: Ekman spirals for exponential thermal wind. *Bound.-Layer Meteor.*, **1**, 137–145.

Melgarejo, J. W., and J. W. Deardorff, 1974: Stability functions for the boundary layer resistance laws based on observed boundary-layer heights. *J. Atmos. Sci.*, **31**, 1324–1333.

Mellor, G. L., 1973: Analytic prediction of the properties of stratified planetary surface layers. *J. Atmos. Sci.*, **30**, 1061–1069.

Schwerdtfeger, W., 1972: The vertical variation of the wind through the friction layer over the Greenland ice cap. *Tellus*, **24**, 13–16.

Sommeria, G., 1976: Three-dimensional simulation of turbulent processes in an undisturbed trade wind boundary layer. *J. Atmos. Sci.*, **33**, 216–241.

Tennekes, H., and J. L. Lumley, 1972: *A First Course in Turbulence*. MIT Press, 300 pp.

Wyngaard, J. C., 1975: Modeling the planetary boundary layer—extension to the stable case. *Bound.-Layer Meteor.*, **9**, 441–460.

——, and O. R. Coté, 1971: The budgets of turbulent kinetic energy and temperature variance in the atmospheric surface layer. *J. Atmos. Sci.*, **28**, 190–201.

Zeman, O., and J. L. Lumley, 1976: Modeling buoyancy driven mixed layers. *J. Atmos. Sci.*, **33**, 1974–1988.

——, and H. Tennekes, 1977: Parameterization of the turbulent energy budget at the top of the daytime atmospheric boundary layer. *J. Atmos. Sci.*, **34**, 111–123.

Zilitinkevich, S. S., 1972: On the determination of the height of the Ekman boundary layer. *Bound.-Layer Meteor.*, **3**, 141–145.

——, 1975: Resistance laws and prediction equations for the depth of the planetary boundary layer. *J. Atmos. Sci.*, **32**, 741–752.

——, and J. W. Deardorff, 1974: Similarity theory for the planetary boundary layer of time-dependent height. *J. Atmos. Sci.*, **31**, 1449–1452.